

# Aerodynamic Drop Breakup Suppression Due To Vaporization

Bradley Boyd<sup>1</sup>, Sid Becker<sup>1</sup>, Yue Ling<sup>2</sup>

<sup>1</sup>University of Canterbury

Private Bag 4800, Christchurch, New Zealand

bradley.boyd@canterbury.ac.nz; sid.becker@canterbury.ac.nz

<sup>2</sup>University of South Carolina

300 Main St, Columbia, USA

stanley\_ling@sc.edu

**Abstract** - The vaporization of a freely moving liquid droplet in a uniform high-temperature gas stream is investigated through direct numerical simulation. The sharp liquid-gas interface is tracked using the geometric Volume-of-Fluid (VOF) method. The incompressible Navier-Stokes equations are solved in conjunction with a two-fluid model for the thermal energy advection and conduction, with an immersed Dirichlet boundary condition at the interface to implicitly account for the latent heat absorption. The model is implemented in the open-source solver, Basilisk, which uses adaptive quadtree/octree mesh for spatial discretization and will allow for adaptive mesh refinement of the region near the interface. An acetone droplet at a moderate Weber number is simulated where the drop deforms into a bag shape and experiences breakup. The rate of vaporization of the drop is then increased to study the influence of vaporization on the drop breakup behaviour. By increasing the rate of vaporization, we observe the suppression of droplet breakup, making an otherwise unstable droplet stable.

**Keywords:** Secondary breakup, Multiphase flow, Atomization, Vaporization, Evaporation, Phase-change

## 1. Introduction

Aerobreakup of vaporizing droplets is commonly seen in a wide variety of industrial applications such as liquid fuel injection, nuclear reactors, and spray cooling, though the interaction between drop aerobreakup and vaporization remains not fully understood. To investigate the fundamental multiphase flow dynamics and phase change involved, the droplet aerobreakup is often studied in an idealized configuration, i.e., a stationary drop is suddenly subjected to a uniform gaseous stream of constant velocity [1], [2]. The morphological change of the drop is controlled by the competition between the destabilizing force, i.e., the inertia of the free gas stream, and the stabilizing forces, such as the surface tension on the gas-liquid interface and the liquid viscous forces. In terms of dimensionless parameters, the key parameters are the Weber ( $We$ ) and the Reynolds ( $Re$ ).

Most of the former studies on drop aerobreakup are through experiments [3]–[7], though high-fidelity interface-resolved simulations have also been reported in recent years [2], [8], [9]. Jain et al. [9] investigated the breakup of drops at moderate Weber numbers, showing the effect of the density ratio and Reynolds number. At moderate Weber numbers, a large range of breakup regimes is observed, including, vibration and bag [9].

When the temperature of the free stream is high, heat and mass transfer will occur when the drop deforms and breaks. Then additional parameters such as the Prandtl number ( $Pr$ ) and the Stefan number ( $St$ ) will arise. The vaporization of a spherical drop in high-temperature environments has been extensively studied experimentally, deriving commonly used empirical relations [10]–[14].

Vaporization of drops at moderate Weber numbers, for which the drops undergo significant deformation and even breakup, did not emerge until very recently in numerical studies [15]. To accurately predict the drop vaporization rate, such highly sophisticated numerical methods are required to rigorously resolve the sharp and vaporizing interface, and these typically employ high mesh resolution to provide well resolved thermal and velocity gas boundary layers near the drop surface. In the recent work by Boyd and Ling [15], a novel volume-of-fluid (VOF) method was proposed, which allows direct numerical simulation of interfacial multiphase flows with phase change, including the aerobreakup of a vaporizing drop at moderate Weber numbers. The volumetric source due to vaporization was added to the pressure equation to account for the non-zero divergence for the velocity near the interface and the resulting Stefan flow. To avoid the perturbation of the

Stefan flow on the velocity at the interfacial cells, a novel treatment was proposed to handle vaporization-induced volumetric source to guarantee that the velocities at the interface cells are correctly represented and can be directly used in VOF advection.

The present study considers the influence of vaporization on droplet dynamics. In the recent work [15], a correlation between droplet deformation and the rate of vaporization was observed. However, no studies to date have considered how vaporization influences drop deformation. First, we present the numerical models and problem description (Section 2). Then we simulate multiple cases of droplet deformation and vary the conditions related to drop vaporization to study the effect of vaporization on the drop evolution (Section 3).

## 2. Numerical Methods

### 2.4. Governing Equations

The incompressible two-phase interfacial flows with vaporization are governed by the Navier-Stokes equations

$$\rho \left( \frac{\partial \mathbf{u}}{\partial t} + \mathbf{u} \cdot \nabla \mathbf{u} \right) = -\nabla p + \nabla \cdot (2\mu \mathbf{D}) + \rho g + \sigma \kappa \delta_\gamma \mathbf{n}_\gamma \quad (1)$$

where  $\mathbf{u}$ ,  $p$ ,  $\mu$ ,  $\rho$ ,  $\sigma$ ,  $\kappa$ ,  $\mathbf{n}_\gamma$ , and  $\delta_\gamma$  are the velocity, pressure, dynamic viscosity, density, surface tension coefficient, curvature, interface normal, and interface Dirac distribution function, respectively. The deformation tensor is defined as  $\mathbf{D} = (\nabla \mathbf{u} + \nabla \mathbf{u}^T)/2$ . Gravity which can be easily included is neglected in the present study.

The one-fluid approach is adopted, in which the two phases are treated as one fluid with properties change abruptly across the interface. The two different phases are distinguished by the volume fraction of the liquid phase  $f$ , which follows the advection equation,

$$\frac{\partial f}{\partial t} + \nabla \cdot (f \mathbf{u}) = -\frac{s_\gamma}{\rho_l} \quad (2)$$

where the subscripts  $l$  and  $g$  denote the liquid and gas properties. The source term on the right accounts for the additional change of the interface location due to phase change, and  $s_\gamma$  is the volumetric source due to phase change, which depends on the mass flux at the interface ( $j_\gamma$ ) and the interfacial area density ( $\phi_\gamma$ ) as  $s_\gamma = j_\gamma \phi_\gamma$ . The interfacial area density is  $\phi_\gamma = A_\gamma/V_c$ , where  $A_\gamma$  is the liquid-gas interface area in a finite-volume cell with a volume  $V_c$ . The mass flux due to phase change,

$$j_\gamma = \frac{1}{h_{l,g}} (k_l \nabla T|_{l,\gamma} \cdot \mathbf{n}_\gamma - k_g \nabla T|_{g,\gamma} \cdot \mathbf{n}_\gamma) \quad (3)$$

is driven by heat transfer, where  $T$ ,  $k$ , and  $h_{l,g}$  are the temperature, thermal conductivity, and specific latent heat of vaporization, respectively. The gas and liquid temperature fields are required to calculate  $j_\gamma$ , which are in turn obtained by solving the energy conservation equation for both the liquid and gas phases [15]–[18]

$$\rho_g c_{p,g} \left( \frac{\partial T_g}{\partial t} + \mathbf{u} \cdot \nabla T_g \right) = \nabla \cdot (k_g \nabla T_g) \quad (4)$$

$$\rho_l c_{p,l} \left( \frac{\partial T_l}{\partial t} + \mathbf{u} \cdot \nabla T_l \right) = \nabla \cdot (k_l \nabla T_l) \quad (5)$$

where  $c_p$  is the isobaric-specific heat. Since  $T_g$  and  $T_l$  are only solved in the gas and liquid regions, the gas-liquid interface is treated as an embedded boundary where the temperature remains as the saturation temperature,  $T_{sat}$ .

The phase change also results in a modification of the continuity equation,

$$\nabla \cdot \mathbf{u} = s_\gamma \left( \frac{1}{\rho_g} - \frac{1}{\rho_l} \right) \quad (6)$$

## 2.4. Numerical Methods and Solvers

The governing equations are solved using a finite volume approach. The advection of the liquid volume fraction (Eq. (2)) is solved using a geometric VOF method [19]. The projection method is used to incorporate the incompressibility condition in the momentum equation, and the pressure Poisson equation is solved using the multi-grid method. The advection of momentum near the interface is conducted in a manner consistent with the VOF advection [15]. The surface tension term in the momentum equation is discretized using the balanced-force continuum-surface-force method [20]. The interfacial curvature that is required for surface tension is calculated using the height-function method [21]. A second-order staggered-in-time discretization of the volume fraction and pressure is used. The quadtree/octree mesh is used to discretize the 2D/3D spatial domains, providing important flexibility to dynamically refine the mesh in user-defined regions. The adaptation criterion is based on the wavelet estimate of the discretization errors of the volume fraction, temperature, and all velocity components.

The energy equations for both phases (Eqs. (4)–(5)) are solved with the Dirichlet boundary condition at the interface, i.e.,  $T_g|_\gamma = T_l|_\gamma = T_{sat}$  which are invoked by setting  $T_g = T_{sat}$  in the cells with  $f > 0$  and  $T_l = T_{sat}$  in the cells with  $f < 1$ . The advection terms are treated similarly to momentum and are consistent with VOF advection, while the diffusion terms are integrated fully implicitly. The determination of  $j_\gamma$  (Eq. (3)) requires the temperature gradient on both the liquid and gas sides of the interface, i.e.,  $\nabla T_g|_\gamma$  and  $\nabla T_l|_\gamma$ . To avoid calculating the gradient across the interface, the temperature gradient for each phase is estimated by extrapolation from the neighbouring pure cells for the corresponding phase. The contribution of vaporization to the interface motion toward the liquid side, i.e., the source term in Eq. (2), is accounted by shifting the planar VOF interface geometrically. As the projection method is used to incorporate the continuity equation, the pressure Poisson equation is solved,

$$\nabla \cdot \left( \frac{\Delta t}{\rho} \nabla p \right) = \nabla \cdot \mathbf{u}^* - \hat{s} \left( \frac{1}{\rho_g} - \frac{1}{\rho_l} \right) \quad (1)$$

where  $\mathbf{u}^*$  is the auxiliary velocity that accounts for all the terms in the momentum equation except the pressure term. Instead of applying the volumetric source  $s_\gamma$  right at the interfacial cell, we distribute the volumetric source to the nearest pure gas cells in a  $5^3$  stencil in 3D ( $5^2$  in 2D). The second term on the right is the additional source term induced by phase change, and  $\hat{s}$  is the sum of the source distribution from all the nearby interfacial cells. The integration of the distributed source  $\hat{s}$  in all pure gas cells is equal to the integration of the volumetric source  $s_\gamma$  over all the interfacial cells. By distributing the volumetric source from the interfacial to the neighbouring gas cells, the velocity in the interfacial cell will not be “contaminated” by the Stefan flow and will remain as the liquid velocity by which the interface moves.

The above numerical methods have been implemented in the open-source solver *Basilisk* [15], [21], [22]. Validation studies of the present methods on two-phase interfacial flows with phase change can be found in our previous studies [15].

## 2.4. Problem description and non-dimensional parameters

We consider a freely moving acetone drop with diameter  $D_0$ , initially stationary and at saturation temperature in an unbounded domain, is suddenly exposed to a uniform superheated stream of vapor of the drop liquid with temperature and velocity  $U_\infty$  (see Figure 1). The properties for the acetone liquid and vapor are provided in Table 1. The  $z$  coordinate chosen to be aligned with the free stream direction. Under the non-zero relative velocity between the drop and the free the drop will be accelerated along the streamwise direction, while in the meantime, it deforms and vaporizes.

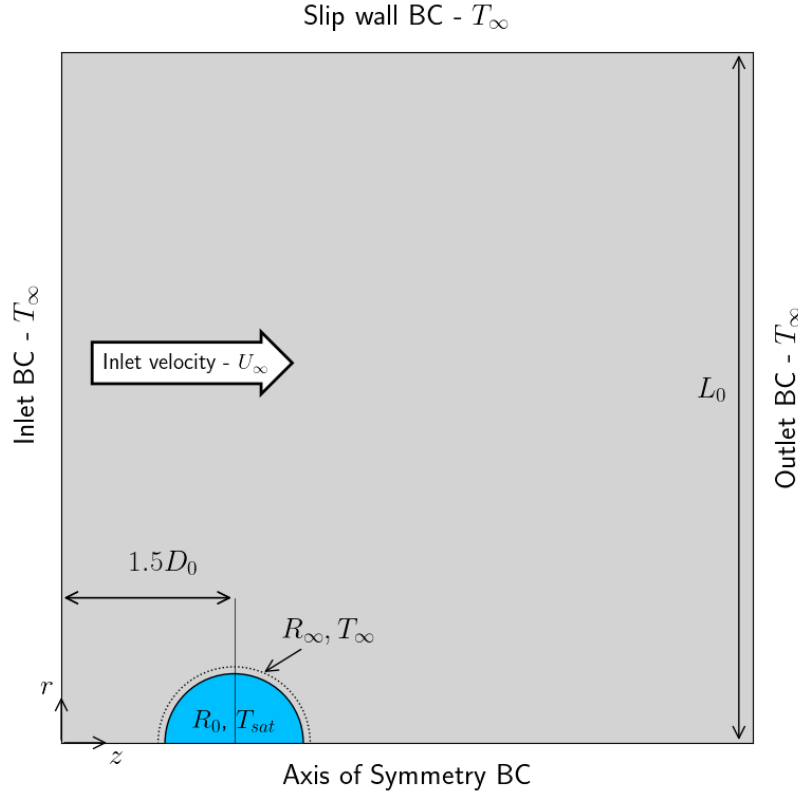


Fig. 1: The computational domain for 2D-axisymmetric simulation of the vaporization of a freely moving drop in a hot vapor stream.

Table 1: Properties of saturated acetone.

Property	$\rho$ [ $kg/m^3$ ]	$k$ [ $W m^{-1}k^{-1}$ ]	$c_p$ [ $W m^{-1} K^{-1}$ ]	$\mu$ [ $Pa s$ ]	$h_{l,g}$ [ $J kg^{-1}$ ]	$T_{sat}$ [ $K$ ]	$\sigma$ [ $N m^{-1}$ ]
Liquid	710	0.156	2420	1.85e-4	4.88e5	359	0.0153
Vapor	5.11	0.0166	1460	9.59e-6	-	-	-

While the gas dynamic pressure tends to destabilize the drop, the surface tension is an important force to resist the deformation. The ratio between the two is represented by the Weber number, which is most commonly used to characterize drop aerobreakup regimes [4]–[6]:  $We = \rho_g U_\infty^2 D_0 / \sigma$ . The Reynolds number, defined as  $Re = \rho_g U_\infty D_0 / \mu_g$ , characterizes the gas flow around the drop, in particular the wake dynamics, which in turn influences the drop deformation and vaporization. Additionally, the rate of vaporization of a drop depends on the Stefan number,  $St = c_{p,g}(T_\infty - T_{sat}) / h_{l,g}$ . The non-dimensional time is as  $t^* = t U_\infty / (D_0 \sqrt{\rho_l / \rho_g})$  [3].

### 3. Results

In the present study, 2D axisymmetric simulations have been performed to investigate the vaporization of a freely moving drop subjected to a uniform hot gas stream. The adaptive quadtree mesh was used to discretize the 2D domain. The mesh resolution is controlled by the maximum level of refinement  $L$ , which corresponds to  $2^L$  cells in each coordinate direction, i.e.,  $L=14$  corresponds to  $2^{14} = 16384$  cells in the  $r$  and  $z$  directions. In the present case we used  $L=14$  for refinement and the length of the computational domain of  $L_0 = 16D_0$ , which gives a minimum cell dimension of  $\Delta z = \Delta r = D_0/1024$ . The mesh adaptation algorithm is based on a wavelet-estimated discretization error [23], [24], where the refinement criterion is based on temperature ( $T$ ), volume fraction ( $f$ ), and velocity ( $\mathbf{u}$ ). In all cases,  $We=35$ ,  $Re=50$ , and the time step is computed based on the  $CFL=0.2$ .

Figure 2(a) shows the streamlines, vaporization rate, and temperature distribution for the acetone droplet early at  $t^* = 0.2$ , where  $St=0.1$ . At this point in time, most of the vaporization occurs on the windward/front surface of the droplet where the temperature gradient is high. On the leeward side of the droplet, a wake is present where the temperature is lower, resulting in less vaporization. As time progresses to  $t^* = 2.6$ , the drop deforms into a bag shape where most of the vaporization occurs on the outer rim of the bag formation, see Figure 2(b).

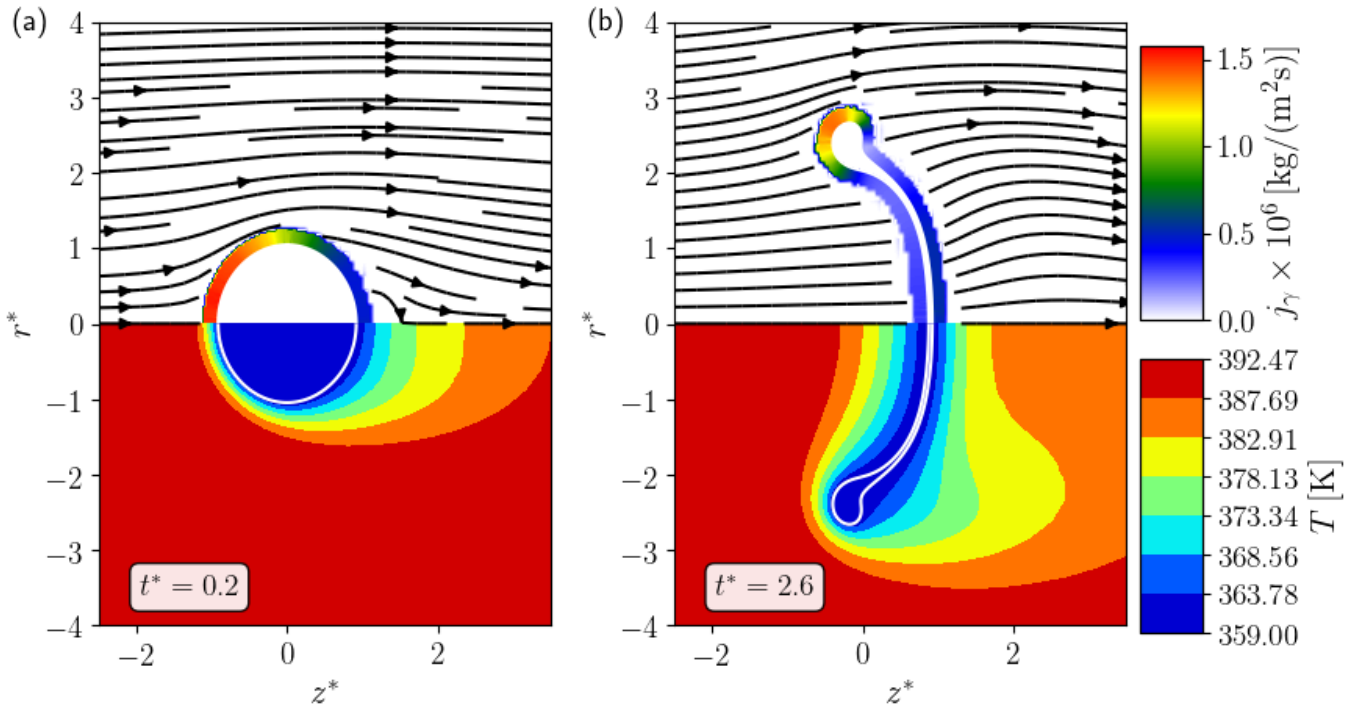


Fig. 2: The (top) streamlines, vaporization rate,  $j_\gamma$ , and (bottom) temperature distribution of the vaporizing acetone droplet at (a)  $t^* = 0.2$  and (b)  $t^* = 2.6$  where  $St=0.1$ ,  $We = 35$  and  $Re = 50$ .

Here, we study the influence of vaporization on drop breakup behaviour. By varying  $St$ , we can consider the influence of the varying rate of vaporization - i.e., increasing  $T_\infty$  increases  $St$  and the vaporization rate. Note that in the case where  $St=2$ ,  $T_\infty \approx 1042$  K. Figure 3(a) shows the evolution of the drop when there is no vaporization occurring ( $St=0$ ). For  $St=0$ , the droplet radially deforms into a disk shape ( $t^* = 1.6$ ). After the disk is formed, a forward bag begins to develop and grow until breakup ( $t^* = 3.6$ ). For  $St=0.1$  and  $0.5$ , the drop still forms a bag, however, the radial deformation is less (Figures 3(a)-(b)). As we continue to increase  $St$ , Figures 3(b)-(g) show that the drop deformation is suppressed so much so that at  $St \geq 1.5$ , the drop no longer breaks. Thus, the droplet is now stable for  $St \geq 1.5$ .

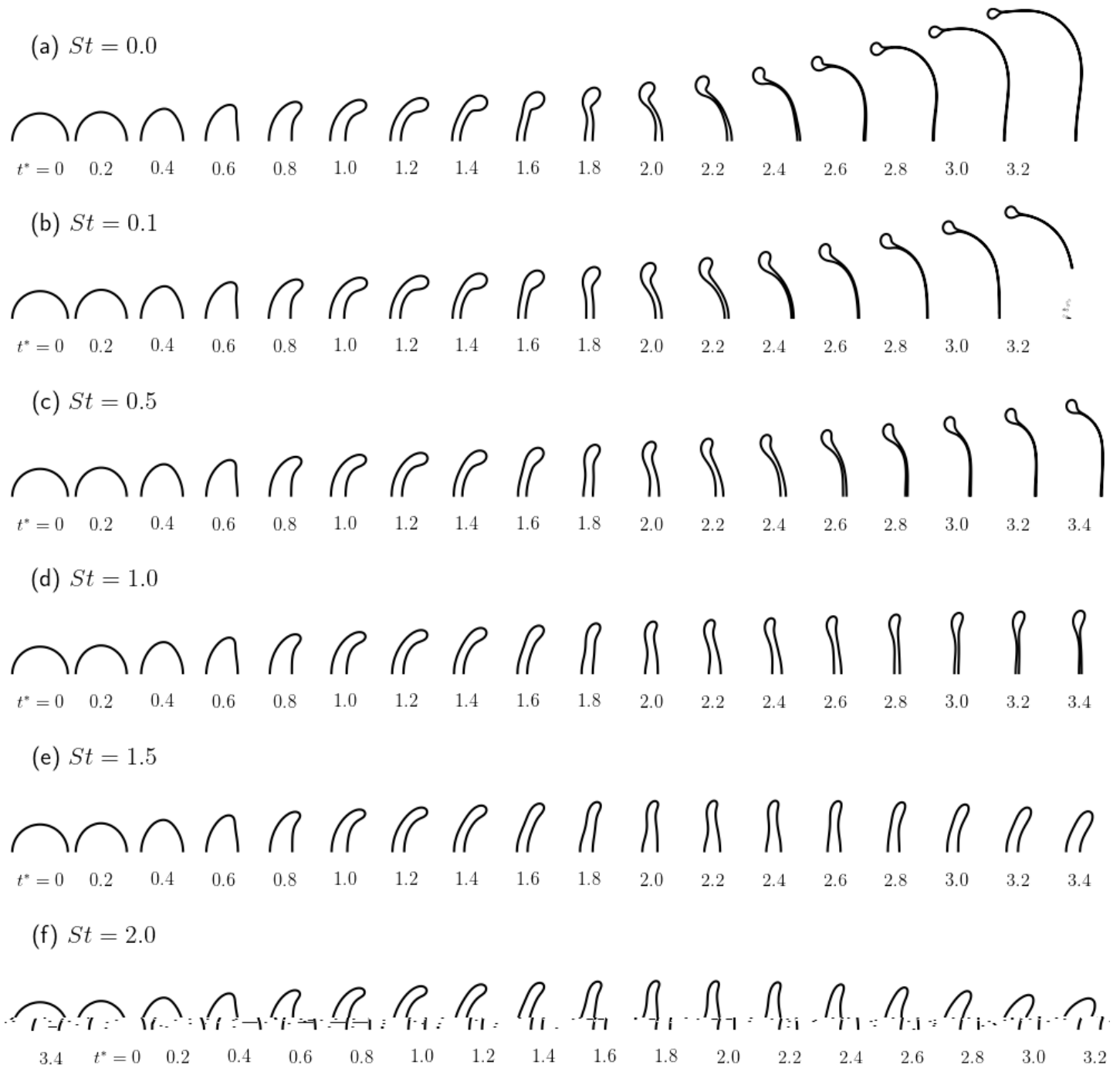


Fig. 3: The temporal evolution of the drop shape ( $We=35$ ) for various Stefan numbers: (a)  $St=0$ , (b) 0.1, (c) 0.5, (d) 1, (e) 1.5, and (f) 2 at  $Re=50$  and  $L14$ .

At the interface of the acetone drop, the dense liquid changes phase to a less dense gas. The increase in volume as the liquid changes phase to gas results in the Stefan flow directed outwards from the interface [15]. The Stefan flow results in a reaction flow on the drop interface which opposed the droplet deformation. This explains why we observed less drop deformation when the rate of vaporization is increased.

To the best of the author's knowledge, the suppression of droplet break due to vaporization has not been previously observed in the literature. This change in droplet breakup behaviour will have an implication for processes such as fuel injection where droplets are experiencing vaporization while undergoing secondary atomization or aerodynamic breakup.

#### 4. Conclusion

The present study considers an impulsively accelerated acetone drop in a high-temperature flow. At the surface of the acetone droplet vaporization from liquid to vapour occurs. In all cases, the droplet Weber number is constant at  $We=35$ , resulting in significant deformation and a bag formation before the breakup when no vaporization occurs ( $St=0$ ). By increasing the vaporization rate, the droplet deforms less and no longer forms a bag ( $St \geq 1.5$ ). Thus, the flow induced by vaporization, referred to as Stefan flow, is significant enough to suppress droplet breakup in the case presented. This behaviour has significant implications for secondary atomization processes where vaporization occurs (i.e., fuel injection).

#### Acknowledgements

This research was supported by the ACS Petroleum Research Fund (#62481-ND9). The authors also acknowledge the Extreme Science and Engineering Discovery Environment (XSEDE) and the Texas Advanced Computing Center (TACC) for providing the computational resources that have contributed to the research results reported in this paper. The Baylor High Performance and Research Computing Services (HPRCS) have been used to process the simulation results. The newly-developed methods have been implemented in the open-source multiphase flow solver *Basilisk*, which is made available by Stephane Popinet and other collaborators.

#### References

- [1] T. G. Theofanous, "Aerobreakup of Newtonian and viscoelastic liquids," *Annual Review of Fluid Mechanics*, vol. 43, pp. 661–690, 2011.
- [2] F. Marcotte and S. Zaleski, "Density contrast matters for drop fragmentation thresholds at low Ohnesorge number," *Physical Review Fluids*, vol. 4, no. 10, p. 103604, Oct. 2019.
- [3] A. A. Ranger and J. A. Nicholls, "Aerodynamic shattering of liquid drops.," *AIAA Journal*, vol. 7, pp. 285–290, 1969.
- [4] B. E. Gelfand, S. A. Gubin, S. M. Kogarko, and S. P. Komar, "Singularities of the breakup of viscous liquid droplets in shock waves," *J. Eng. Phys.*, vol. 25, pp. 1140–1142, 1975.
- [5] L.-P. Hsiang and G. M. Faeth, "Near-limit drop deformation and secondary breakup," *International Journal of Multiphase Flow*, vol. 18, pp. 635–652, 1992.
- [6] T. G. Theofanous and G. J. Li, "On the physics of aerobreakup," *Physics of Fluids*, vol. 20, no. 5, p. 052103, May 2008.
- [7] S. Sharma, A. Pratap Singh, S. Srinivas Rao, A. Kumar, and S. Basu, "Shock induced aerobreakup of a droplet," *Journal of Fluid Mechanics*, vol. 929, p. A27, Dec. 2021.
- [8] J. C. Meng and T. Colonius, "Numerical simulation of the aerobreakup of a water droplet," *Journal of Fluid Mechanics*, vol. 835, p. 1108, 2018.
- [9] S. S. Jain, N. Tyagi, R. S. Prakash, R. V. Ravikrishna, and G. Tomar, "Secondary breakup of drops at moderate Weber numbers: Effect of Density ratio and Reynolds number," *International Journal of Multiphase Flow*, vol. 117, pp. 25–41, Aug. 2019.
- [10] M. Renksizbulut and M. C. Yuen, "Experimental study of droplet evaporation in a high-temperature air stream," *Journal of Heat Transfer*, vol. 105, no. 2, pp. 384–388, May 1983.
- [11] S. S. Sazhin, "Advanced models of fuel droplet heating and evaporation," *Progress in Energy and Combustion Science*, vol. 32, no. 2, pp. 162–214, Jan. 2006.

- [12] R. J. Haywood, R. Nafziger, and M. Renksizbulut, “A detailed examination of gas and liquid phase transient processes in convective droplet evaporation,” *Journal of Heat Transfer*, vol. 111, no. 2, pp. 495–502, May 1989.
- [13] C. H. Chiang, M. S. Raju, and W. A. Sirignano, “Numerical analysis of convecting, vaporizing fuel droplet with variable properties,” *International Journal of Heat and Mass Transfer*, p. 18, 1992.
- [14] M. C. Yuen and L. W. Chen, “Heat-transfer measurements of evaporating liquid droplets,” *International Journal of Heat and Mass Transfer*, vol. 21, no. 5, pp. 537–542, May 1978.
- [15] B. Boyd and Y. Ling, “A consistent volume-of-fluid approach for direct numerical simulation of the aerodynamic breakup of a vaporizing drop,” *Computers & Fluids*, p. 105807, 2023.
- [16] Y. Sato and B. Ničeno, “A sharp-interface phase change model for a mass-conservative interface tracking method,” *Journal of Computational Physics*, vol. 249, pp. 127–161, Sep. 2013.
- [17] L. Bureš and Y. Sato, “Direct numerical simulation of evaporation and condensation with the geometric VOF method and a sharp-interface phase-change model,” *International Journal of Heat and Mass Transfer*, vol. 173, p. 121233, Jul. 2021.
- [18] L. C. Malan, A. G. Malan, S. Zaleski, and P. G. Rousseau, “A geometric VOF method for interface resolved phase change and conservative thermal energy advection,” *Journal of Computational Physics*, vol. 426, p. 109920, Feb. 2021.
- [19] G. D. Weymouth and D. K.-P. Yue, “Conservative Volume-of-Fluid method for free-surface simulations on Cartesian-grids,” *Journal of Computational Physics*, vol. 229, no. 8, pp. 2853–2865, Apr. 2010.
- [20] M. M. Francois, S. J. Cummins, E. D. Dendy, D. B. Kothe, J. M. Sicilian, and M. W. Williams, “A balanced-force algorithm for continuous and sharp interfacial surface tension models within a volume tracking framework,” *Journal of Computational Physics*, vol. 213, pp. 141–173, 2006.
- [21] S. Popinet, “An accurate adaptive solver for surface-tension-driven interfacial flows,” *Journal of Computational Physics*, vol. 228, no. 16, pp. 5838–5866, Sep. 2009.
- [22] S. Popinet, “Gerris: a tree-based adaptive solver for the incompressible Euler equations in complex geometries,” *Journal of Computational Physics*, vol. 190, no. 2, pp. 572–600, Sep. 2003.
- [23] S. Popinet, “A quadtree-adaptive multigrid solver for the Serre–Green–Naghdi equations,” *Journal of Computational Physics*, vol. 302, pp. 336–358, Dec. 2015.
- [24] J. A. van Hooft, S. Popinet, C. C. van Heerwaarden, S. J. A. van der Linden, S. R. de Roode, and B. J. H. van de Wiel, “Towards adaptive grids for atmospheric boundary-layer simulations,” *Boundary-Layer Meteorology*, vol. 167, no. 3, pp. 421–443, Jun. 2018.